Thermally Stable, Adhesively Strong Graphene/Polyimide Films for Inkjet Printing Ultrasound Sensors

Pengyu Zhou[a], Yaozhong Liao[b], Xiongbin Yang[a], Yiyin Su[a], Jianwei Yang[a],

Lei Xu[a], Kai Wang[c], Zhihui Zeng[d], Li-min Zhou[e], Zhong Zhang[f], Zhongqing Su[a,g]*

[a] Department of Mechanical Engineering,

The Hong Kong Polytechnic University, Kowloon, Hong Kong SAR

[b] School of Aerospace Engineering,

Xiamen University, Xiamen 361102, PR China

[c] Department of Aeronautical and Aviation Engineering,

The Hong Kong Polytechnic University, Kowloon, Hong Kong SAR

[d] Swiss Federal Laboratories for Materials Science and Technology (Empa),

Dübendorf 8600, Switzerland

[e] School of System Design and Intelligent Manufacturing,

Southern University of Science and Technology, Shenzhen 518055, PR China

[f] CAS Key Laboratory of Nanosystem and Hierarchical Fabrication,

National Center for Nanoscience and Technology, Beijing 100190, PR China

[g] The Hong Kong Polytechnic University Shenzhen Research Institute

Shenzhen 518057, P.R. China

submitted to *CARBON*

(initially submitted on 28th May 2021; revised and resubmitted on 20th July 2021)

* To whom correspondence should be addressed. Tel.: +852-2766-7818, Fax: +852-2365-4703,
Email: zhongqing.su@polyu.edu.hk (Prof. Zhongqing Su, *Ph.D.*)

32   **Abstract**

33   Targeting for flexible, broadband ultrasound sensors, a new breed of nanographene platelet

34   (NGP)/polyimide (PI) film is inkjet printed with morphologically optimized NGP/poly (amic

35   acid) hybrid-based nanocomposite ink. The ink is produced with high-shear liquid phase

36   exfoliation from inexpensive bulk graphite, manifesting good printability and high graphene

37   concentration as high as 13.1 mg mL^{-1}. Featuring an ultra-thin thickness ($\sim$ 1 μm only), the

38   inkjet-printed NGP/PI film sensor is demonstrated to possess excellent thermal stability and

39   high adhesive strength reaching the American Society for Testing and Materials 5B level.

40   The highly uniform and consolidated NGP/PI nanostructure in the sensor enables the

41   formation of π-π interaction between NGPs and PI polymer matrix, and the quantum

42   tunneling effect is triggered among NGPs when ultrasound traverses the sensor. This sensing

43   mechanism endows the NGP/PI sensor with good sensitivity, fidelity and accuracy, showing

44   comparable performance as prevailing commercial ultrasound sensors such as piezoelectric

45   sensors. The film sensor has a proven gauge factor as high as 739, when sensing ultrasound

46   at 175 kHz, and a ultrabroad responsive spectrum up to 1.6 MHz.

47

48   *Keywords*: inkjet-printed sensor, liquid exfoliation, graphene, polyimide, high frequency

49   ultrasound

50

51   **1. Introduction**

52   High frequency ultrasound plays an irreplaceable role in a broad spectrum of applications,

53   from super-resolution ultrasound imaging for cardiovascular pathology [1], through acoustic

54   tweezers for manipulating microparticles [2] and ultrasound-guided drug delivery [3], to

55   high-precision contactless nondestructive evaluation for jet turbine blade surfaces [4].

56   Prevailing sensors for perceiving high frequency ultrasound are produced with piezoelectric

57　materials owing to the high transduction efficiency, broadband responsivity and high

58　sensitivity that the materials have, as typified by inorganic piezoelectric materials (typically

59　lead zirconate titanate (PZT) ceramics) [5], piezoelectric polymer polyvinylidene fluoride

60　(PVDF) and its copolymer with fluoride-trifluoroethylene (PVDF-TrFE) [6]. Nevertheless,

61　PZT ceramics are known rigid and unwieldy, presenting difficulty conforming to a curved

62　surface, and the lead-rich components make the biocompatibility questionable [7]. Flexible

63　lead-free PVDF renders good sensing coverage over an extended area, and can adapt to

64　curved surfaces, but its sensitivity to ultrasound signals of high frequency is inferior, as a

65　result of its lower piezoelectric coefficient compared with PZT ceramics [8]. Driven by

66　demanding applications today, such as flexible healthcare wearables that are functionable in

67　an ultrasound regime, the concurrent amelioration of ultrasound sensors on sensing accuracy,

68　broadband, sensitivity, as well as conformability has been a core of recent research foci.

69

70　Graphene – the two-dimensional (2D) allotrope of carbon, shows alluring intrinsic properties

71　in terms of charge carrier concentration and mobility [9], thermal conductivity [10],

72　mechanical strength [11], chemical stability [12], and flexibility [13]. With these appealing

73　merits, graphene-based nanocomposites have opened up a new way for developing

74　innovative electronic devices and sensors in particular [14]. To name but a few, the piezo-

75　response of single-layer graphene (SLG) grown via chemical vapor deposition (CVD) on

76　Si/SiO_2 calibration grating substrates was investigated, which demonstrates a high

77　piezoelectric effect ($d_{33} \approx 1.4$ nm V^{-1}) of SLG on Si/SiO_2 substrates [15]. Graphene-based

78　cellular elastomers with reduced graphene oxide (rGO) were fabricated, and thus-produced

79　elastomers could provide instantaneous and high-fidelity electrical response to dynamic

80　pressures up to 2 kHz [16]. Graphene oxide (GO)/graphene resistive pressure sensors were

81　produced, with proven capability of responding to transient signals up to 10 kHz [17]. These

3

82 studies are among pioneering exploration in recent years, which has affirmed the capability

83 of graphene-based nanocomposites in sensing dynamic strains, and paved a solid path

84 leading to flexible, functional devices for acquiring high frequency ultrasound signals.

85

86 Central to development of graphene-based ultrasound sensors, using direct-write approaches

87 such as inkjet printing, is the formulation and preparation of graphene-based ink. Amidst

88 diverse techniques for producing graphene, the liquid phase exfoliation (LPE), allowing

89 graphene flakes to be isolated directly from inexpensive natural bulk graphite, outperforms

90 many others by virtue of its operational simplicity, effectiveness but low cost. Solution

91 processability of LPE makes it possible to develop compatible, chemically stable inks for

92 direct writing – a cost-effective additive manufacturing technique that can be used for

93 fabricating large-scale, flexible devices directly on various substrates [18]. However, when

94 used to prepare inks for inkjet printing a sensing device, the conventional LPE by sonication

95 may be inadequate to render satisfactory dispersion stability, concentration, production

96 quality and efficiency. These deficiencies of conventional LPE are among some key barriers

97 to preclude the rapid and scalable production of inkjet-printable, graphene-based inks with

98 good quality and functionality [19].

99

100 In this study, we present a new breed of nanographene platelet (NGP)/polyimide (PI) film

101 for producing flexible, ultrasensitive ultrasound sensors via drop-on-demand inkjet printing.

102 The graphene-based ink is made with NGP/poly (amic acid) (PAA) hybrid nanocomposites

103 that are prepared using novel high-shear LPE, in which few-layer NGPs are exfoliated from

104 inexpensive bulk graphite. The ink features remarkable concentration of NGP as high as 13.1

105 mg mL^{-1}, and presents good printability, storage stability, and functionality, with which the

106 inkjet-printed flexible NGP/PI film sensor has an ultra-thin thickness of ~ 1 μm only, along

107   with excellent thermal stability and adhesive strength reaching the American Society for

108   Testing and Materials (ASTM) 5B level (*i.e.*, the highest level of adhesion grade). With a

109   highly uniform and consolidated NGP/PI nanostructure in the sensor, quantum tunneling

110   effect is triggered among NGPs and π-π interaction is formed between NGPs and PI polymer

111   matrix, endowing the sensor with a gauge factor as high as 739 when responding to

112   ultrasound at 175 kHz, and a broad sensing band from zero to 1.6 MHz.

113

114   **2. Experimental Section**

115   **2.1. Nanocomposite Sensing Ink Fabrication and Characterization**

116   Ethyl cellulose (EC, viscosity 4 cP, 5 % in toluene/ethanol, Aldrich Chemistry; 0.2 g) and

117   polyvinylpyrrolidone (PVP, PVP K-30, Sigma-Aldrich; 0.3 g) are dissolved in N-methyl-2-

118   pyrrolidone (NMP, anhydrous, Aladdin; 100 mL) at a room temperature (25 °C). Then, bulk

119   graphite powder (Aladdin®; 2.0 g) is mixed with the solvent using high shear laboratory

120   mixer (L5M, Silverson®) at 6,000 rpm for 1 h, followed with centrifugation (H1850, Cence®)

121   at 5,000 rpm (2,655 × *g*) for 20 min to remove unexfoliated graphite particles, and the

122   supernatant containing exfoliated few-layer NGPs is collected as NGP ink. To produce the

123   ink, PAA solution (12.8 wt% (80% NMP/20% aromatic hydrocarbon), Sigma-Aldrich; 1.6

124   g) is added into the as-prepared NGP ink (20 mL). The mixture is magnetically stirred at 800

125   rpm for 30 min, and then filtered through a 0.22 µm-diameter PVDF micropore sieve to

126   screen larger agglomerates. The density of the NGP/PAA ink is estimated by weighing a

127   certain volume of the filtered ink using a pipette, and its viscosity is measured by a

128   viscosimeter (NDJ-5S, Lichen Technology). The surface tension measurement of the solvent

129   and ink is conducted using a force tensiometer (K100, KRÜSS®). The NMP solvent surface

130   energy (E_{Sur}^{Sol}) is calculated via $E_{Sur}^{Sol} = \gamma + TS_{Sur}^{Sol}$ [20], where γ refers to the measured surface
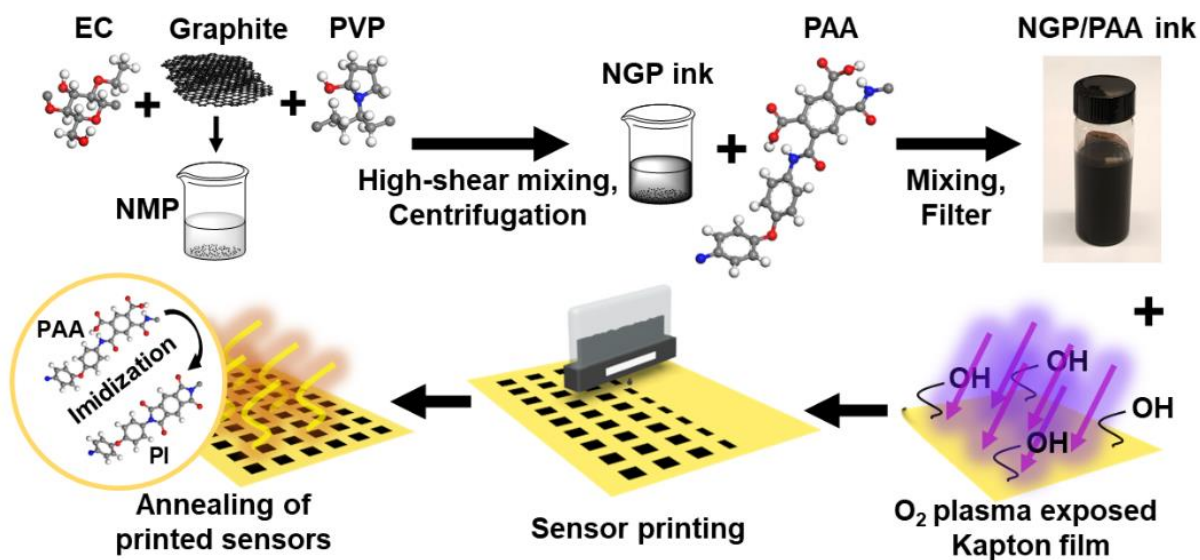
131   tension of NMP solvent, T the temperature, and S_{Sur}^{Sol} the solvent surface entropy (universal

132   value of ~ 0.1 mJ m^{-2} K^{-1}), respectively. The morphology of exfoliated few-layer NGPs is

133   characterized by field emission scanning electron microscopy (FESEM, MAIA 3,

134   TESCAN®) and atomic force microscopy (AFM, AC mode, scan rate 0.8 Hz, MFP-3D

135   Infinity, Asylum, OXFORD INSTRUMENTS®). For FESEM and AFM sample preparation,

136   0.02 vol% NGP ink (10 μL) is drop-casted onto pre-heated Si/SiO$_2$ substrates (250 °C),

137   followed by annealing at 200 °C for 30 min. For UV-vis sample preparation, the ink is diluted

138   to 0.1 vol% to avoid scattering loss [21], and the UV-vis spectra are obtained using a UV-

139   vis double beam spectrophotometer (DB-20, Halo).

140

141   **2.2. Sensor Printing, Imidization, and Characterization**

142   NGP/PAA ink is directly printed on a Kapton (PI) film (25 μm thick) using a PiXDRO LP50

143   inkjet printer (OTB Solar-Roth & Rau) equipped with a DMC-11610 cartridge (Dimatix-

144   Fujifilm Inc.). Before the printing process, the Kapton film is pre-treated with O$_2$ plasma

145   using a plasma cleaner (PDC-002, Harrick Plasma, Inc.) for 2 min at 450 mTorr. The sensors

146   are printed at a room temperature, under a driving voltage of 28 V with driving frequency of

147   4 kHz, and the printing resolution is set as 500 dpi in both in-scan and cross-scan directions.

148   During the printing process, the printer substrate temperature is set as 40 °C to reduce

149   "coffee-stain" effect. After printing, sensors are transferred onto a hot plate and annealed at

150   380 °C for 30 min, for complete solvent evaporation, stabilizer decomposition, and PAA

151   imidization. The fabrication process of the inkjet-printed, film-type NGP/PI ultrasound

152   sensor is recapped in **Figure 1**. The morphology of the printed sensors is characterized using

153   FESEM (MAIA 3, TESCAN®). The thickness and surface roughness of the sensors are

154   measured with a surface profiler (DektakXT surface optical profiler, Bruker®). The electrical

155   resistance (R) of the sensors is measured using a four-probe method on a dynamic digital

multimeter (4-wire resistance mode, DMM 7510, Keithley[®]), with a correction factor of 2.4575 [22]. The electrical conductivity (σ) of the sensors is calculated via $\sigma = l/(R \cdot A)$, where l and A are the length and effective cross-section area of the sensor, respectively. For Fourier-transform infrared spectroscopy (FTIR), Raman and X-ray photoelectron spectroscopy (XPS) characterization, the sensors are printed onto silicon wafer substrates with the same printing condition. FTIR spectra are obtained with a Bruker[®] VERTEX 70 FTIR spectrometer, and Raman spectra are recorded with a Raman spectrometer (488 nm excitation laser wavelength, LabRAM HR 800, HORIBA[®]). XPS spectra are obtained with an XPS system (Thermo Fisher[®] Nexsa). Thermogravimetric analysis (TGA) is performed using a TGA/DSC3+ (Mettler Toledo[®]) system from room temperature to 800 $^\circ$C under an argon or air flow at 80 mL min^{-1}, with a heating rate of 10 $^\circ$C min^{-1}. ASTM D3359 adhesion test (cross-cut tape test) is conducted with Elcometer[®] ASTM D3359 adhesive tape [23].

Figure 1. Schematic of the fabrication process of inkjet printing the film-type NGP/PI ultrasound sensor with optimized NGP/PAA nanocomposite ink.

174

2.3. Calibration of Ultrasound Sensing Capability

The excitation ultrasound signal is generated with a waveform generator based on NI® PXIe-1071 platform and amplified by a Ciprian® US-TXP-3 linear power amplifier, taking a waveform of five-cycle Hanning-function-modulated sinusoidal tone-bursts with the central frequency ranging from 100 to 1,600 kHz (with a stepping of 25 kHz). A glass fiber/epoxy composite laminate plate (600 mm long and wide, and 1 mm thick) is prepared, and a lead stibium niobium (PSN)-33 piezoelectric wafer as an ultrasound actuator is surface-bonded at the center of the plate. The excitation signal is applied on the PSN-33 wafer to introduce an ultrasound signal into the plate. To examine the ultrasound sensing capability of the inkjet-printed NGP/PI nanocomposite sensors, eight printed sensors are silver-pasted with electrodes and surface-mounted on the plate, 50 and 150 mm away from the PSN-33 actuator (four sensors for each sensing distance), respectively. For each printed sensor, a PSN-33 wafer is collocated alongside the sensor for signal comparison and strain calibration. The printed sensor is instrumented to a self-developed signal amplification module which comprises a resistance-voltage (R-V) transformation system [24]. Such a module converts piezoresistive variations to electrical signals, and the converted ultrasound signals and their counterpart signals captured by the PSN-33 piezoelectric wafers (amplified by a Ciprian® low noise pre-amplifier) are recorded simultaneously with an oscilloscope (DSO 9064A, Agilent®). The electrical resistances of electrical cables and connections in the measurement system are negligible.

3. Results and Discussion

The nanocomposite ink is formulated with NGP/PAA, in which NMP is chosen as the solvent, due to the similarity in surface energy between NMP (74.5 mJ m^{-2}) and graphite (~ 70-80 mJ

199   m^{-2}), leading to a near-to-zero enthalpy for exfoliation of graphite. As a result of the low

200   enthalpy, a very small net energetic cost is required, making it possible to achieve effective

201   exfoliation of graphite and stable dispersion of graphene through an LPE process [20].

202   Graphite is exfoliated and dispersed in the solvent via a high-shear LPE process. EC and

203   PVP are selected as polymeric stabilizer and rheology modifier, to prevent re-aggregation

204   and precipitation of exfoliated NGPs. Compared with conventional sonication-based LPE,

205   this fabrication here shows additional merits including higher production quality and

206   efficiency. The operation of high-shear LPE is precisely controlled, followed with a

207   centrifugation process to minimize the possibility of printer nozzle clogging by unexfoliated

208   particles of larger dimensions during the inkjet printing. **Figures 2(a)** and **2(b)** depict the

209   morphology of typical NGPs exfoliated from bulk graphite via FESEM and AFM. **Figure**

210   **2(c)** shows the statistic result of NGP dimensions via AFM measurement, to observe that

211   73.3% of the NGPs are of an ultra-thin thickness smaller than 3 nm, and most of the NGPs

212   present a platelet length of 50-200 nm – that is significantly smaller than 1/50 of the diameter

213   of DMC-11610 printing nozzle (*i.e.*, 430 nm), adequate to avoid printing nozzle blockage.

214
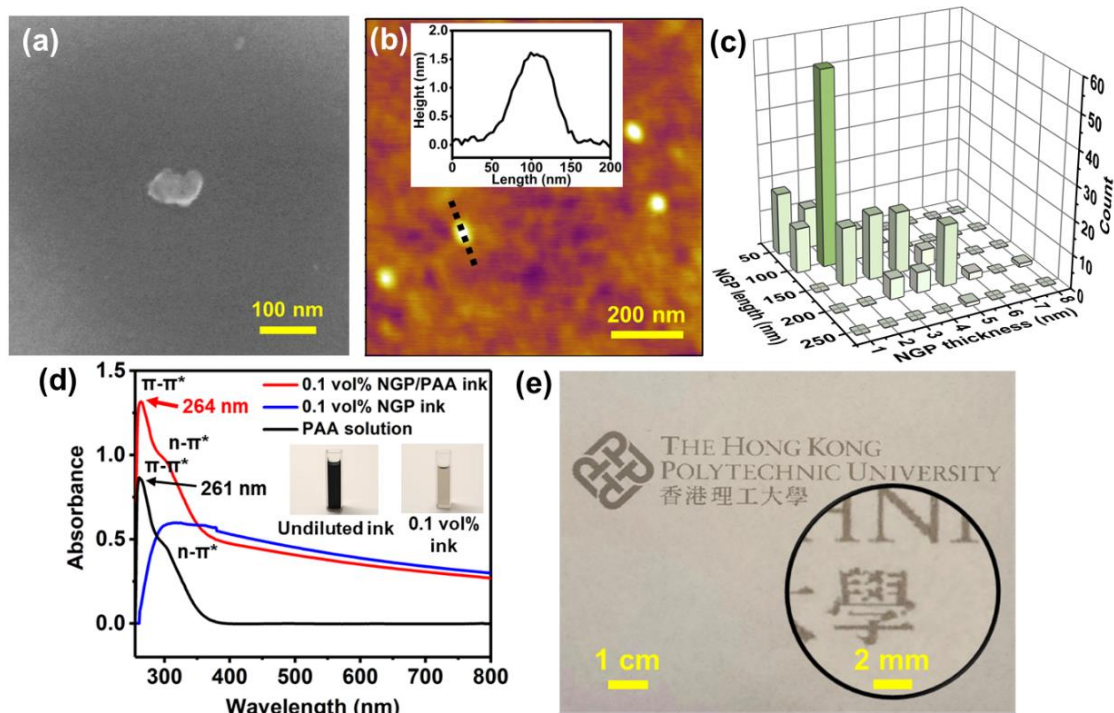
Figure 2. (a) FESEM and (b) AFM images of NGPs exfoliated by high-shear LPE (insert in (b): height profile of a typical NGP). (c) Statistic result of NGP dimensions via AFM measurement. (d) UV-vis spectra of the NGP/PAA nanocomposite ink (0.1 vol%), NGP ink (0.1 vol%) and PAA solution (inserts: undiluted and 0.1 vol% NGP/PAA inks in quartz cuvettes). (e) An illustrative pattern printed with the NGP/PAA ink on a piece of ordinary paper, showing fine printing details.

Targeting for an inkjet-printed sensor that is able to respond to ultrasound in a broad regime, PI is selected as the polymeric matrix of the sensor with twofold consideration: (i) PI, a versatile polymer with aromatic structure connected with imide linkage in its backbone, is of good flexibility and heat resistance. Compared with conventional polymeric matrices used for developing ultrasound sensors (*e.g.*, PVDF and PVP), PI possesses lower dielectric constant, yet higher glass transition temperature and extraordinary thermal stability. The aromatic moieties of PI are of a high degree of similarity to that of the carbon structure in

231   graphene, despite that PI is intrinsically insulative. The interaction between PI and graphene

232   facilitates responsivity and sensitivity of the fabricated sensor to high frequency ultrasound

233   (to be discussed later in this section); and (ii) PAA – the precursor of PI, is miscible with

234   NMP solvent – a trait that is vitally important to warrant uniform, homogeneous and stable

235   dispersion of NGPs in the ink.

236

237   With selected nanoparticles and polymetric matrix, the concentration of NGPs in NGP/PAA

238   ink is estimated according to the UV-vis spectrum of the ink (**Figure 2(d)**) with the Beer-

239   Lambert law [25]

$$A_\lambda = \alpha_\lambda c l , \qquad\qquad (1)$$

240   where A_λ signifies the absorption of ink at wavelength λ, α_λ the absorption coefficient at λ, c

241   the concentration of NGPs, and l the path length of the spectroscopy. With $\alpha_{660nm} = 2,460$ L

242   g^{-1} m^{-1} [20], the NGP concentration of the prepared NGP/PAA ink is estimated, using

243   Equation (1), to be 13.1 mg mL^{-1}, which remarkably exceeds the minimum threshold of the

244   graphene concentration (*i.e.,* 1 mg mL^{-1}) to ensure adequate printing efficiency – as

245   suggested elsewhere [26].

246

247   Notably, after 3-month of storage at a room temperature, the ink is observed to remain its

248   original morphology with no obvious precipitation of NGP. Such excellent storage stability

249   of the ink is verified by UV-vis spectroscopy (**Figure S1**), in which A_{660nm} of the NGP/PAA

250   ink still remains 98% after three months of storage.

251

252   To evaluate the printability of the prepared nanocomposite ink, a figure of merit – Z which

253   is the inverse of Ohnesorge number (O_h) [27], is introduced to calculate the capability of the

254   ink of generating stable droplets during the inkjet printing process. Z reads

$$Z = \frac{1}{O_{\mathrm{h}}} = \frac{(\gamma \rho d)^{1/2}}{\eta} , \qquad (2)$$

255   where γ denotes the surface tension of the ink, ρ the ink density, η the ink viscosity, and d

256   the nozzle diameter (21.5 μm for DMC-11610 nozzle used in this study). To ensure good

257   printability of the ink, and in the meantime avoid viscosity dissipation and satellite drops, Z

258   shall preferably fall into the optimal range between 1 and 10 [27]. Key physical properties

259   of the NGP/PAA ink are listed in **Table S1**, and Z of the prepared ink is calculated to be 6.5

260   – a value that implies excellent compatibility and appropriateness of the NGP/PAA ink for

261   inkjet printing. Thus-produced ink exhibits satisfactory concentration of NGPs, excellent

262   storage stability yet good printability.

263

264   Thus-formulated and prepared NGP/PAA ink is directly printed on substrates using a

265   PiXDRO LP50 inkjet printer. The good printability of the ink can further be confirmed via

266   the droplet which is captured with a stroboscopic camera equipped on the printer (**Figure**

267   **S2**). Representative NGP/PAA ink droplets generated from a printing nozzle of the DMC-

268   11610 cartridge are shown in **Figure S2**, and the droplets are observed stable during jet-

269   printing without any satellite droplet. To demonstrate the printing performance of the ink

270   with a better contrast, an illustrative paradigm printed with the ink on a piece of ordinary

271   paper is shown in **Figure 2(e)**, in which fine printing details are depicted clearly,

272   demonstrating that excellent printing quality and fine resolution can be achieved with the

273   optimized ink.

274

275   Prior to sensor printing, a Kapton film substrate is pre-treated with O_2 plasma to create

276   hydrophilic functional groups on the surface, increasing substrate surface energy and

277   improving the wettability and printing quality of the ink when it is deposited on the substrate.

278   As shown in **Figure 3(a)**, the inkjet-printed NGP/PI nanocomposite sensors deposited on the

279   Kapton film substrate manifest good flexibility. After fully folding the sensor, the electrical

280   resistance of the sensor slightly varies by 2.51% only, and no obvious defect or crack can be

281   observed on the sensor. As can be seen from the FESEM images, **Figures 3(b)-(d)** and **S3**,

282   NGPs are evenly distributed in PI matrix, in close proximity with others. Such a homogenous

283   nanostructure serves as a building block for creating a stable and uniform electrical-

284   conductive network in the sensor, conducive to triggering the tunneling effect when

285   ultrasound traverses the sensor.

286
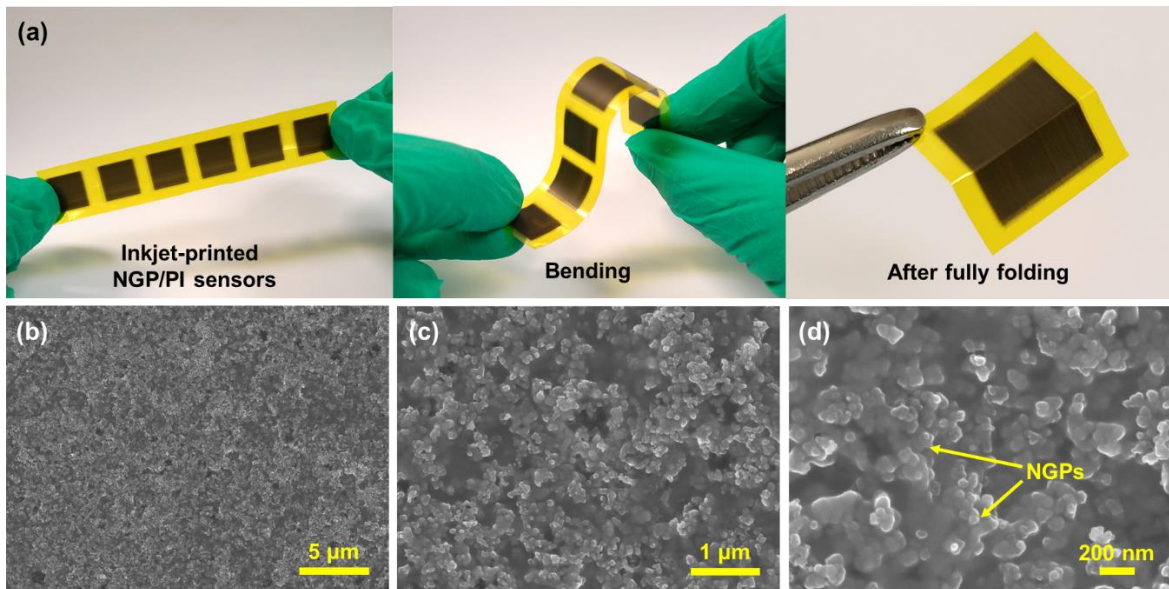
287

288

289   **Figure 3.** (a) Inkjet-printed NGP/PI sensors on Kapton film substrates. (b)-(d) FESEM

290   images of the inkjet-printed NGP/PI sensor.

291

292   FTIR analysis is conducted for the printed NGP/PI sensor, and spectra obtained before and

293   after annealing are compared in **Figure 4(a)**. The FTIR spectrum before annealing shows

294   typical characteristic infrared absorption bands of C=O (COOH) stretching vibration at 1713

295   cm^{-1}, C=O (CONH) stretching vibration at 1637 cm^{-1} (amide I band), C–NH vibration at

296   1540 cm^{-1} (amide II band), and symmetric C=C stretching vibration of aromatic ring at 1490

297   cm^{-1}; in the spectrum of annealed NGP/PI sensor, the characteristic bands at 1776 and 1712

298   cm^{-1} are assigned to symmetric and asymmetric C=O stretching vibration, respectively.

299   Absorption band at 1492 cm^{-1} is attributed to the symmetric C=C stretching vibration of

300   aromatic ring, and the band at 1361 cm^{-1} is due to the C–N stretching of imide ring [28]. The

301   appearance of imide C–N band (1361 cm^{-1}) and absence of amide I and II bands articulate

302   the complete *in-situ* imidization of PAA in the annealed NGP/PI sensor. Raman spectra of

303   the printed NGP/PI sensor before and after annealing are displayed in **Figure 4(b)**, to

304   observe two broad and intense peaks. Peak I of the NGP/PAA hybrid (1343 cm^{-1})

305   corresponds to the D peak of graphitic carbon atoms in NGP, and it shifts to 1365 cm^{-1} after

306   the annealing process, as peak I of the imidized NGP/PI sensor is the overlap of the D peak

307   and the peak of C–N stretching vibration of the imide ring [29]. Peak II in the spectra is

308   produced by the overlapping among G peak of graphitic carbon atoms in NGP, and the peaks

309   of original and imidized aromatic ring vibration of PI [30]. The intensity ratio of the peak II

310   and peak I (I_{II}/I_{I}) increases after annealing, indicating reduced intrinsic microstructural

311   defect in the printed sensor.

312

313   Aromatic moieties in PI chains are of a high degree of similarity to the hexagonal carbon

314   structure of graphene, and when there is an overlap exist between aromatic groups, π-π

315   stacking interaction occurs [31]. During ink preparation, after the high-shear LPE, the free

316   surface of NGP becomes much larger and π-π interaction is consequently formed between

317   the greatly extended NGP aromatic system and aromatic moieties of PAA. This can be

318   verified from UV-vis spectroscopy, as shown in **Figure 2(d)**. In **Figure 2(d)**, both NGP/PAA

319   ink and PAA solution exhibit an absorption peak, while there is no meaningful peak in the

320   spectrum of NGP ink, as the peak is attributed to the electronic transitions of benzene. The

321   maximum absorption wavelength (λ_{max}) of the NGP/PAA ink (264 nm) is larger than that of

322 the pristine PAA solution (261 nm), and the red shift in the figure suggests the formation of

323 π-π interaction between the high-shear exfoliated NGPs and PAA polymer [32]. The

324 existence of π-π interaction also renders the ink with good storage stability. After sensor

325 printing and annealing, by virtue of the nondestructive and reversible nature of π-π

326 interaction, π-π interaction exists between the π-π* electron cloud of NGPs and the π

327 electrons of aromatic moieties of PI (**Figure 4(c)**).

328

329

330
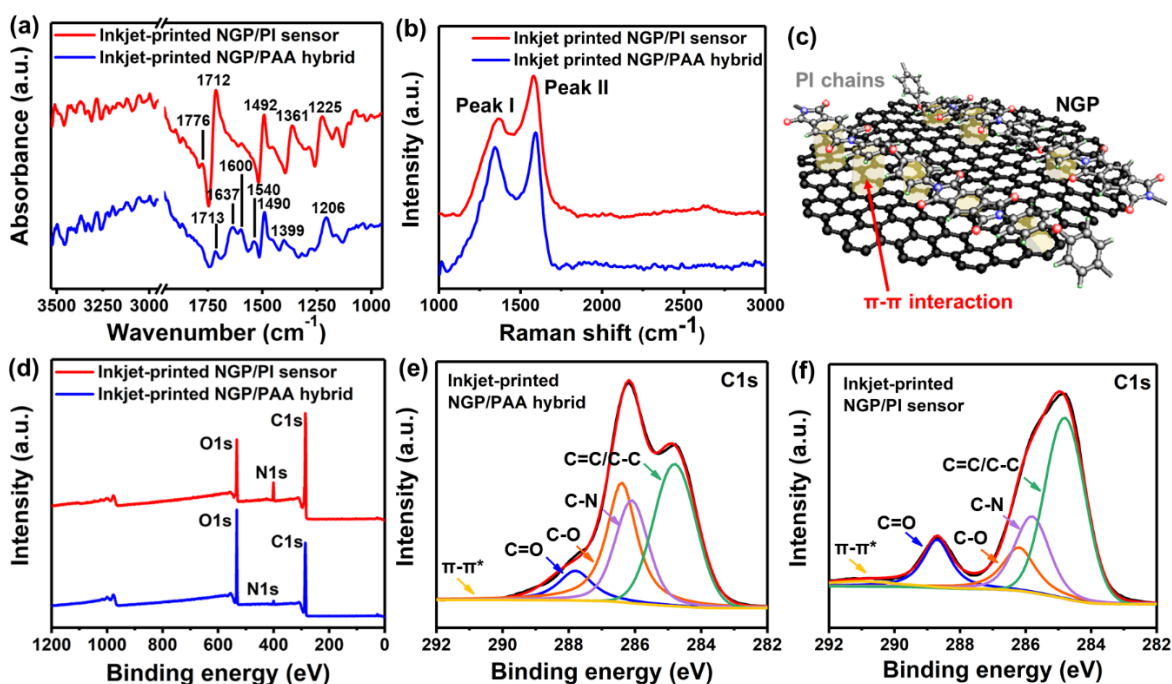
331 **Figure 4.** (a) FTIR, and (b) Raman spectra of inkjet-printed NGP/PAA hybrid (before

332 annealing) and NGP/PI sensor (after annealing). (c) Schematic illustration of π-π

333 interaction between NGPs and PI chains. (d) XPS spectra of inkjet-printed NGP/PAA

334 hybrid (before annealing) and NGP/PI sensor (after annealing). (e) XPS spectra for C1s of

335 inkjet-printed NGP/PAA hybrid (before annealing), and (f) NGP/PI sensor (after

336 annealing).

337

338   To gain a deeper insight into the chemical and structural characteristics of the printed NGP/PI

339   sensor, the NGP/PI sensor is characterized with XPS. EC, PVP and PI polymers are also

340   characterized with XPS (**Figure S4**). The XPS spectrum of the printed NGP/PI

341   nanocomposite sensor exhibits an intense C1s peak (**Figure 4(d)**), accompanied by a weaker

342   O1s peak after annealing, suggesting a high sp^2-hybridized carbon content ratio. **Figures 4(e)**

343   and **4(f)** compare the C1s spectra of the sensor before and after annealing. As can be seen

344   from the spectra, both the peak intensities of C–N and C–O bonds decrease remarkably after

345   the annealing process, while the peak intensity of sp^2-hybridized carbon content augments,

346   indicating the decomposition of EC and PVP stabilizer, as well as a consolidated NGP/PI

347   nanostructure in the sensor. Key parameters including electrical conductivity, thickness, and

348   surface roughness of the sensor before and after the annealing process are presented in **Table**

349   **S2**. The printed sensor features an ultra-thin thickness of ~ 1 μm (see **Figure S5** for detailed

350   results of thickness measurement). The annealed NGP/PI sensor presents a thinner thickness

351   and smaller surface roughness, yet a better electrical conductivity than the unannealed

352   NGP/PAA hybrid (**Table S2**), as a result of the complete imidization of PAA and removal of

353   EC and PVP after the annealing process.

354

355   Thermal stability of the inkjet-printed NGP/PI sensor is scrutinized with TGA, with results

356   shown in **Figure 5(a)**. With PI as its polymeric matrix, the onset degradation temperature of

357   the printed sensor is as high as 500 and 560 ºC, respectively in air and in argon, suggesting

358   excellent intrinsic thermal stability of the sensor. Adhesive strength between the printed

359   NGP/PI sensor and the Kapton substrate is evaluated with a standard adhesion test

360   conforming with ASTM D3359 [23]. **Figure 5(b)** shows the sensor and the tape after the

361   ASTM D3359 cross-cut tape test, to observe that no any content of the sensor is removed

362   from the substrate after the tape is peeled off, arguing that adhesion has reached an ASTM

363   5B level, *viz.*, the highest level of adhesion grade. The superb adhesive strength of the sensor

364   is attributed to the hydrogen bonds formed between carbonyl groups of PI matrix and

365   hydrophilic functional groups on the O_2 plasma pre-treated Kapton substrate.

366
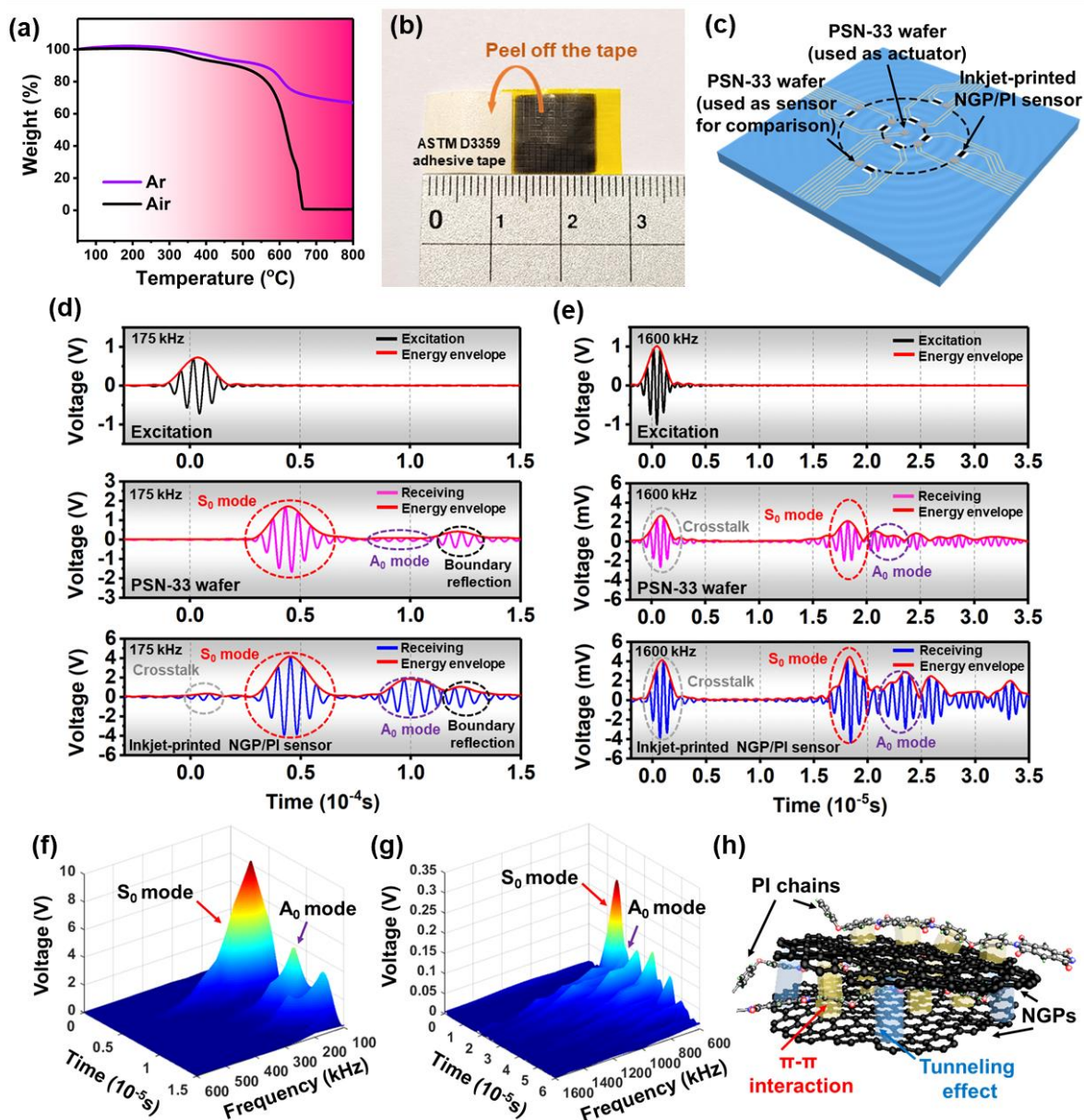
367

368

369   **Figure 5.** (a) TGA curves of inkjet-printed NGP/PI sensor. (b) The inkjet-printed NGP/PI

370   sensor and adhesive tape after ASTM D3359 cross-cut tape test. (c) Schematic of

371   experimental set-up for ultrasound acquisition. (d) Excitation signal, and ultrasound signals

17

372   captured by the PSN-33 wafer and by inkjet-printed NGP/PI sensor, at 175 kHz, and (e) at

373   1,600 kHz. (f) Signals captured by NGP/PI sensor in a sweep range from 100 to 600 kHz,

374   and (g) from 600 to 1,600 kHz. (h) Schematic illustration of the ultrasound sensing

375   mechanism of the printed NGP/PI sensor.

376

377   The sensing capability of the inkjet-printed NGP/PI nanocomposite sensor is interrogated

378   and calibrated in a broad frequency range up to megahertz, with experimental details in

379   Section 2.3. A PSN-33 piezoelectric wafer is surface-glued at the center of a glass

380   fiber/epoxy composite laminate (600 mm long and wide, and 1 mm thick), **Figure 5(c)**, for

381   exciting an ultrasound signal in a sweep frequency ranging from 100 to 1,600 kHz. A group

382   of eight NGP/PI nanocomposite sensors are surface-adhered on the laminate for signal

383   acquisition, collocated to each of which is a PSN-33 wafer for comparison and calibration.

384   For ultrasound signals in the frequency range of 100-600 kHz, the sensing distance is 150

385   mm (using the four NGP/PI sensors and four PSN-33 sensors located along the outer circle,

386   see **Figure 5(c)**), while the sensing distance is decreased to 50 mm (both types of sensors

387   along the inner circle) for signals beyond 600 kHz. The reason of selecting different

388   measurement distances with regard to different ultrasound frequencies is that an ultrasound

389   signal of higher frequency attenuates quicker than that of a lower frequency, and the

390   shortened measurement distance for signals beyond 600 kHz is conducive to remain an

391   adequate signal-to-noise ratio. As some representative results, **Figure 5(d)** comparably

392   displays the raw ultrasound signals captured by the printed NGP/PI sensor and the PSN-33

393   wafer at 175 kHz, to observe that the first-arrival wave component (*viz.*, the zeroth-order

394   symmetric Lamb wave mode guided by the laminate, denoted by S_0 mode hereinafter) in

395   signals perceived by the printed sensor is in quantitative agreement with that captured by the

396   PSN-33 wafer in terms of the arrival time. In addition, the zeroth-order anti-symmetric Lamb

18

397   wave mode (A_0) following the S_0 mode, is also perceived faithfully and accurately by the

398   printed sensor. It is noteworthy that the signal magnitudes of these two sensors cannot be

399   directly compared due to the different sensing mechanisms: the printed sensors are a type of

400   piezoresistive sensors, while the PSN-33 sensors are based on piezoelectric measurement.

401   **Figure 5(e)** displays the signals captured by both types of sensors under an excitation of

402   1,600 kHz, which are filtered by a fast Fourier transformation-based algorithm to reduce

403   crosstalk and noise. The printed sensor is observed to maintain its high degree of sensitivity,

404   fidelity, and precision at such a high frequency.

405

406   To examine the effect of annealing on sensing capacity, signals captured by the NGP/PAA

407   hybrid (namely before annealing) and by the NGP/PI sensor (*viz.*, after annealing) are

408   compared in **Figure S6.** As can be seen from **Figure S6**, the signal magnitude for NGP/PAA

409   hybrid at 175 kHz is lower than that for NGP/PI sensor, implying that the consolidated

410   nanostructure after imidization without residual solvent and polymer stabilizer (EC and PVP)

411   plays a critical role in enhancing the ultrasound sensing performance.

412

413   **Figures 5(f)**, **5(g)**, **S7(a)** and **S7(b)** compare signals captured by the NGP/PI sensor and

414   PSN-33 wafer over the time-frequency domain, respectively, from 100 to 1,600 kHz. In such

415   a broad frequency regime, both sensors show high consistency. These findings articulate that

416   printed NGP/PI sensors faithfully perceive broadband ultrasound, with comparable

417   performance as that of a commercial piezoelectric sensor, yet with additional merits

418   including flexibility, lightweight and rapid prototyping. Such excellent ultrasound sensing

419   performance is attributed to its consolidated nanostructure established by NGPs and PI. As

420   commented earlier, with the developed NGP/PAA nanocomposite ink and the drop-on-

421   demand inkjet printing fabrication process, NGPs are distributed evenly in PI polymeric

422   matrix of the sensor, forming a stable and uniform electrical-conductive network. As is

423   known that quantum tunneling effect can be triggered between adjacent conductive

424   nanoparticles in an insulating polymer when the nanoparticles are in close proximity with

425   others [33]. When the printed sensor is subject to ultrasound-induced high-frequency

426   dynamic strains, such a disturbance is usually too weak to break up the electrical-conductive

427   network formed in the sensor, which, however, is adequate to alter the distance between

428   adjacent NGPs, leading to the variation of tunneling condition of charged carriers and the

429   change in tunneling resistance among NGPs. It is noteworthy that the π-π interaction formed

430   in the sensor can accelerate the charge carrier transfer between NGPs and PI [34], but π-π

431   interaction is not as strong as covalent bonding or electrostatic interaction. The consequence

432   is that when ultrasound traverses the sensor, the particulate movement of NGPs also affects

433   the binding force and charge transfer of π-π interaction between NGPs and PI matrix (**Figure**

434   **5(h)**), and this becomes an additional factor to amplify the variation of tunneling resistance

435   between NGPs and engender the strong and accurate response of the NGP/PI sensor to high

436   frequency ultrasound.

437

438   To put it into perspective, the gauge factor (K) of the printed sensor, in responding to

439   ultrasound, is calculated as [35]

$$K = \frac{\Delta R}{R_0} / \varepsilon = \frac{R_x - R_0}{R_0} / \varepsilon \, , \qquad (3)$$

440   where ΔR is the resistance change of the printed NGP/PI sensor, R_x the resistance of the

441   printed sensor under a high-frequency ultrasound signal, R_0 the intrinsic resistance of the

442   printed sensor, and ε the ultrasound-induced dynamic strain. $\Delta R/R_0$ is calculated in terms of

443   the mechanism of the R-V circuit in the self-developed signal amplification module. The

444   mechanism of the R-V circuit depicts a relationship linking the ultrasound signal magnitude

445   (peak-to-peak value) measured by the sensor (V_o) to R_x, as [24]

$$\frac{V_O}{Amp} = V_S(\frac{R_x}{R_x + R_0} - \frac{R_1}{R_1 + R_0}),\qquad(4)$$

where *Amp* is the amplification scale of the module (1,385 times gain amplification at the current excitation frequency of 175 kHz), V_s the power source voltage (10 V in this study), and R_1 the resistance of the variable reference resistor in the R-V circuit. In the experiment, R_1 is adjusted to be the same as R_0 to warrant the maximal sensitivity [24]. With Equation (4), $\Delta R/R_0$ is calculated as 2.89×10^{-3}. As mentioned earlier in Section 2.3, for each printed sensor, a PSN-33 piezoelectric wafer is collocated alongside the printed sensor for signal comparison and strain calibration. The magnitudes of ultrasound-induced dynamic strains applied to these two types of sensors are considered the same, and ε is calculated via [36]

$$\varepsilon = \frac{V_P d_{31}(1-k_{31}^2)}{tk_{31}^2},\qquad(5)$$

where V_P denotes the peak-to-peak value of the responsive voltage of PSN-33 piezoelectric wafer adjacent to the NGP/PI sensor, d_{31} the in-plane piezoelectric coefficient of the wafer, k_{31} the electromechanical coupling coefficient of the wafer, and *t* the thickness of the wafer. With the key parameters of the PSN-33 wafer in **Table S3**, ε is determined as 3.91×10^{-6} at 175 kHz, and *K* is calculated as 739 via Equation (3). Such an extraordinarily high gauge factor of the inkjet-printed NGP/PI sensor verifies its excellent sensing performance to high frequency ultrasound – a result that has never been achieved by the prevailing nanocomposite sensors.

4. Conclusion

A new breed of NGP/PI-based film is developed with novel NGP/PAA ink, for fabricating ultrasensitive ultrasound sensors using inkjet printing. The novel graphene-based ink is cost-effectively produced with facile high-shear LPE directly from inexpensive bulk graphite,

467 exhibiting advantages of high graphene concentration, good storage stability, inkjet
468 printability yet good functionality. The tailor-made printed film sensor features an ultra-thin
469 thickness (~ 1 μm), excellent thermal stability and extraordinary adhesive strength (ASTM
470 5B level). By virtue of the uniform and compact nanostructure in the sensor, the quantum
471 tunneling effect triggered among NGPs, and π-π interactions formed between NGPs and PI
472 endow the printed sensor with a gauge factor as high as 739 (at 175 kHz). The sensor has
473 proven capability of accurately sensing ultrasound in a regime of megahertz (up to 1.6 MHz).
474 This new type of flexible, ultrasensitive sensor features not only extraordinary sensitivity,
475 fidelity, and sensing precision that are comparable to commercial piezoelectric wafer, but
476 also additional merits including light weight, low cost, large-scale production, and
477 fabrication mildness and simplicity, highlighting its alluring potential of being expanded to
478 other application domains such as wearable healthcare devices for ultrasound-based disease
479 diagnosis.

480

487

488 **References**

489 [1] K. Ozawa, J.R. Lindner, Ultrasound Molecular Imaging: Insights into Cardiovascular
490 Pathology, Journal of Echocardiography 18(2) (2020) 86-93.

491 [2] C.R.P. Courtney, C.E.M. Demore, H. Wu, A. Grinenko, P.D. Wilcox, S. Cochran, *et al.*

492 Independent Trapping and Manipulation of Microparticles Using Dexterous Acoustic

493 Tweezers, Applied Physics Letters 104(15) (2014) 154103.

494 [3] S. Mullick Chowdhury, T. Lee, J.K. Willmann, Ultrasound-Guided Drug Delivery in

495 Cancer, Ultrasonography 36(3) (2017) 171-184.

496 [4] F. Mevissen, M. Meo, A Review of NDT/Structural Health Monitoring Techniques for

497 Hot Gas Components in Gas Turbines, Sensors 19(3) (2019).

498 [5] F. Lanza di Scalea, S. Salamone, Temperature Effects in Ultrasonic Lamb Wave

499 Structural Health Monitoring Systems, The Journal of the Acoustical Society of America

500 124(1) (2008) 161-174.

501 [6] Y. Li, W. Feng, L. Meng, K.M. Tse, Z. Li, L. Huang, *et al.* Investigation on In-Situ

502 Sprayed, Annealed and Corona Poled PVDF-TrFE Coatings for Guided Wave-Based

503 Structural Health Monitoring: From Crystallization to Piezoelectricity, Materials & Design

504 199 (2021) 109415.

505 [7] M.T. Chorsi, E.J. Curry, H.T. Chorsi, R. Das, J. Baroody, P.K. Purohit, *et al.*

506 Piezoelectric Biomaterials for Sensors and Actuators, Advanced Materials 31(1) (2019)

507 1802084.

508 [8] V. Cauda, S. Stassi, K. Bejtka, G. Canavese, Nanoconfinement: an Effective Way to

509 Enhance PVDF Piezoelectric Properties, ACS Applied Materials & Interfaces 5(13) (2013)

510 6430-6437.

511 [9] M. Yoonessi, J.R. Gaier, M. Sahimi, T.L. Daulton, R.B. Kaner, M.A. Meador,

512 Fabrication of Graphene-Polyimide Nanocomposites with Superior Electrical Conductivity,

513 ACS Applied Materials & Interfaces 9(49) (2017) 43230-43238.

514 [10] T. Wu, Y. Xu, H. Wang, Z. Sun, L. Zou, Efficient and Inexpensive Preparation of

515 Graphene Laminated Film with Ultrahigh Thermal Conductivity, Carbon 171 (2021) 639-

516 645.

517 [11] G.-H. Lee, R.C. Cooper, S.J. An, S. Lee, A. van der Zande, N. Petrone, *et al.* High-

518 Strength Chemical-Vapor-Deposited Graphene and Grain Boundaries, Science 340(6136)

519 (2013) 1073.

520 [12] F. Torrisi, T. Carey, Graphene, related two-dimensional crystals and hybrid systems for

521 printed and wearable electronics, Nano Today 23 (2018) 73-96.

522 [13] Z. Mu, T. Liu, X. Ji, H. Luo, L. Tang, S. Cheng, A Facile and Cost-Effective Approach

523 to Fabricate Flexible Graphene Films for Aqueous Available Current Collectors, Carbon 170

524 (2020) 264-269.

525 [14] M.T. Tran, T.T. Tung, A. Sachan, D. Losic, M. Castro, J.F. Feller, 3D Sprayed

526 Polyurethane Functionalized Graphene/Carbon Nanotubes Hybrid Architectures to Enhance

527 the Piezo-resistive Response of Quantum Resistive Pressure Sensors, Carbon 168 (2020)

528 564-579.

529 [15] G. da Cunha Rodrigues, P. Zelenovskiy, K. Romanyuk, S. Luchkin, Y. Kopelevich, A.

530 Kholkin, Strong Piezoelectricity in Single-Layer Graphene Deposited on SiO_2 Grating

531 Substrates, Nature Communications 6(1) (2015) 7572.

532 [16] L. Qiu, M. Bulut Coskun, Y. Tang, J.Z. Liu, T. Alan, J. Ding, *et al.* Ultrafast Dynamic

533 Piezoresistive Response of Graphene-Based Cellular Elastomers, Advanced Materials 28(1)

534 (2016) 194-200.

535 [17] S. Liu, X. Wu, D. Zhang, C. Guo, P. Wang, W. Hu, *et al.* Ultrafast Dynamic Pressure

536 Sensors Based on Graphene Hybrid Structure, ACS Applied Materials & Interfaces 9(28)

537 (2017) 24148-24154.

538 [18] P. He, B. Derby, Inkjet Printing Ultra-Large Graphene Oxide Flakes, 2D Materials 4(2)

539 (2017) 021021.

540 [19] K.R. Paton, E. Varrla, C. Backes, R.J. Smith, U. Khan, A. O'Neill, *et al.* Scalable

541 Production of Large Quantities of Defect-Free Few-Layer Graphene by Shear Exfoliation in

542 Liquids, Nature Materials 13(6) (2014) 624-630.

543 [20] Y. Hernandez, V. Nicolosi, M. Lotya, F.M. Blighe, Z. Sun, S. De, *et al.* High-Yield

544 Production of Graphene by Liquid-Phase Exfoliation of Graphite, Nature Nanotechnology

545 3(9) (2008) 563-568.

546 [21] T. Juntunen, H. Jussila, M. Ruoho, S. Liu, G. Hu, T. Albrow-Owen, *et al.* Inkjet Printed

547 Large-Area Flexible Few-Layer Graphene Thermoelectrics, Advanced Functional Materials

548 28(22) (2018) 1800480.

549 [22] F.M. Smits, Measurement of Sheet Resistivities with the Four-Point Probe, The Bell

550 System Technical Journal 37(3) (1958) 711-718.

551 [23] ASTM International. Standard Test Methods for Rating Adhesion by Tape Test; ASTM

552 D3359-17; West Conshohocken, PA, 2017.

553 [24] Z. Su, L. Zhou, L. Qiu, H. Xu, Z, Zeng, M. Liu. Resistance-Voltage Transformation

554 System for Sensors in Dynamic Strain Measurement and Structural Health Monitoring. US

555 Patent (2018) 9 863 824 B1.

556 [25] T. Pandhi, E. Kreit, R. Aga, K. Fujimoto, M.T. Sharbati, S. Khademi, *et al.* Electrical

557 Transport and Power Dissipation in Aerosol-Jet-Printed Graphene Interconnects, Scientific

558 Reports 8(1) (2018) 10842.

559 [26] S. Majee, M. Song, S.-L. Zhang, Z.-B. Zhang, Scalable Inkjet Printing of Shear-

560 Exfoliated Graphene Transparent Conductive Films, Carbon 102 (2016) 51-57.

561 [27] F. Torrisi, T. Hasan, W. Wu, Z. Sun, A. Lombardo, T.S. Kulmala, *et al.* Inkjet-Printed

562 Graphene Electronics, ACS Nano 6(4) (2012) 2992-3006.

563 [28] S. Diaham, M.L. Locatelli, T. Lebey, D. Malec, Thermal Imidization Optimization of

564 Polyimide Thin Films Using Fourier Transform Infrared Spectroscopy and Electrical

565 Measurements, Thin Solid Films 519(6) (2011) 1851-1856.

566 [29] Y. Qin, Q. Peng, Y. Ding, Z. Lin, C. Wang, Y. Li, *et al.* Lightweight, Superelastic, and

567 Mechanically Flexible Graphene/Polyimide Nanocomposite Foam for Strain Sensor

568 Application, ACS Nano 9(9) (2015) 8933-8941.

569 [30] Y. Seo, S.M. Lee, D.Y. Kim, K.U. Kim, Kinetic Study of the Imidization of a Poly(ester

570 amic acid) by FT-Raman Spectroscopy, Macromolecules 30(13) (1997) 3747-3753.

571 [31] S. Grimme, Do Special Noncovalent π–π Stacking Interactions Really Exist?,

572 Angewandte Chemie International Edition 47(18) (2008) 3430-3434.

573 [32] Q. Wang, Y. Bai, Y. Chen, J. Ju, F. Zheng, T. Wang, High Performance Shape Memory

574 Polyimides Based on π–π Interactions, Journal of Materials Chemistry A 3(1) (2015) 352-

575 359.

576 [33] N. Hu, Y. Karube, C. Yan, Z. Masuda, H. Fukunaga, Tunneling Effect in a

577 Polymer/Carbon Nanotube Nanocomposite Strain Sensor, Acta Materialia 56(13) (2008)

578 2929-2936.

579 [34] Y. Hsun Su, Y. Kai Wu, S.L. Tu, S.-J. Chang, Electrostatic Studies of π–π Interaction

580 for Benzene Stacking on a Graphene Layer, Applied Physics Letters 99(16) (2011) 163102.

581 [35] H. Gullapalli, V.S.M. Vemuru, A. Kumar, A. Botello-Mendez, R. Vajtai, M. Terrones,

582 *et al.* Flexible Piezoelectric ZnO–Paper Nanocomposite Strain Sensor, Small 6(15) (2010)

583 1641-1646.

584 [36] V. Giurgiutiu, Chapter 7 - Piezoelectric Wafer Active Sensors – PWAS Transducers,

585 in: V. Giurgiutiu (Ed.), Structural Health Monitoring with Piezoelectric Wafer Active

586 Sensors (Second Edition), Academic Press, Oxford, 2014, pp. 357-394.

587